

3D OPTICAL PROFILOMETRY WITH A DOUBLE BEAM-SPLITTER SETUP

by

İsra Merve Çetin

B.S., Physics, Boğaziçi University, 2017



Submitted to the Institute for Graduate Studies in
Science and Engineering in partial fulfillment of
The requirements for the degree of
Master of Science

Graduate Program in Physics

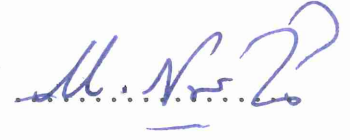
Boğaziçi University

2019

3D OPTICAL PROFILOMETRY WITH A DOUBLE BEAM-SPLITTER SETUP

APPROVED BY:

Prof. M. Naci İnci
(Thesis Supervisor)



Prof. M. Burçin Ünlü



Prof. Gülen Aktaş Greenwood



DATE OF APPROVAL: 02.08.2019

ACKNOWLEDGEMENTS

I would like to thank my thesis supervisor Professor M. Naci İnci for all the encouragement and guidance throughout the study of my MSc thesis and providing the opportunity to study with him and engagement through the learning process of this master thesis.

I would like to extent my thanks to my laboratory colleagues, Miss Belkıs Gökbulut, Mrs Sema Güvenç and Dr Ekrem Yartaşı for their support, valuable suggestions and most importantly for their precious friendship during my studies. I would like to thank especially Mr Arda İnanç for his patience, belief and support.

Finally, I would like to thank my family and my fiancé, who encouraged me for everything and supported me with their love. I will be grateful forever for their support and endless patience. My special thanks to my brother Mr İsrail Çetin who has a special place in my life.

ABSTRACT

3D OPTICAL PROFILOMETRY WITH A DOUBLE BEAM-SPLITTER SETUP

In this thesis, it is demonstrated that a double beam splitter arrangement is very convenient and more practical to generate square shaped fringe patterns, and fringe distribution can be easily controlled in two dimensions. This enables to extract 3D height distribution of test objects without using any additional component as a projection unit.

To approve the validity of the proposed technique, various frequencies of the fringe pattern are obtained by rotating a cubic beam splitter, and images that include deformed fringe patterns due to the height distribution of test objects are captured by a CCD camera. The resultant square fringe pattern is analyzed with two-dimensional continuous wavelet transform method and is separated into two fringe patterns in horizontal and vertical axes with a certain algorithm. The height-related phase map is acquired after analysis process.

ÖZET

ÇİFT IŞIK BÖLÜCÜ DÜZENEĞİ İLE 3 BOYUTLU OPTİK PROFİLOMETRE

Bu tezde, çift ışık bölücü düzeneğinin kare saçak deseni üretimi için uygun ve pratik olduğu, ayrıca saçak dağılımının iki boyutta kolayca kontrol edilebileceği gösterildi. Bu yöntem, üç boyutlu test objelerinin yükseklik dağılımının ilave herhangi bir projeksiyon ünitesi kullanılmaksızın elde edilmesine imkân sağladı.

Önerilen tekniğin geçerliliğini kanıtlamak için, küp şeklindeki ışık bölücünün açısı değiştirilerek çeşitli frekanslarda saçak desenleri elde edildi ve test objelerinin yükseklik dağılımından dolayı deforme olan saçak desenlerini içeren görüntüler CCD kamera ile yakalandı. Oluşan kare saçak desenleri iki boyutlu sürekli dalgacık dönüşümü metodu kullanılarak analiz edildi ve belirli bir algoritma ile dikey ve yatay eksenlerdeki iki saçak desenine ayrıştırıldı. Analiz sonunda yüksekliğe bağlı faz haritası elde edildi.

TABLE OF CONTENTS

ACKNOWLEDGEMENTS	iii
ABSTRACT	iv
ÖZET	v
LIST OF FIGURES	viii
LIST OF SYMBOLS/ABBREVIATIONS	xi
1. INTRODUCTION	1
2. REVIEW	3
2.1. Generation Methods for Square-Shaped Fringe Pattern.	3
2.1.1. Lloyd’s Double Mirror Interferometer	3
2.1.2. Optical Fiber System	5
2.1.3. Moiré Pattern with Grating and Digital Fringe Projection.	9
2.2. Analysis Method for Square-Shaped Fringe Pattern	10
2.2.1. Two-dimensional Continuous Wavelet Transform	10
3. EXPERIMENTAL.	17
3.1. Set-up	17
3.2. Gates’ Interferometry and Double Beam-Splitter	18
4. ANALYSIS	20
4.1. Algorithm to Separate Fringe Patterns	20
4.1.1. Ridge Extraction & Construction of a Reliability Map	22
4.1.2. Phase Unwrapping Procedure.	23
4.1.3. Removing Carrier Frequency	26

4.2. Results and Discussion 28

 4.2.1. Flower Shaped Object. 27

 4.2.2. Object with Steps 30

5. CONCLUSION. 33

REFERENCES 35



LIST OF FIGURES

Figure 2.1. Square-shaped pattern is captured by CDD camera in the dark room	3
Figure 2.2 Lloyd' mirror alignment with a single mirror.	4
Figure 2.3. Lloyd's Double Mirror set-up and interference of two fringe patterns by using four fiber sources [9]	5
Figure 2.4. Three optical fiber system for fringe projection	6
Figure 2.5. Formation of square shaped fringe pattern with four core optical fiber system	6
Figure 2.6. Moiré pattern generation[13]	9
Figure 2.7. Scheme for a digital fringe pattern image processing system. [14].	10
Figure 3.1. Sketch of our experimental set-up.	18
Figure 3.2. Gates' interferometer was sketched by CAD design tool, Tinkercad	19
Figure 3.3. Gates' interferometer show transmission and reflection of incident rays [30].	19
Figure 3.4. Double beam splitter arrangement for interferometric measurements.	20
Figure 4.1. A complex fringe pattern[31]	21
Figure 4.2.a and 4.2.b: Horizontal and vertical phase components of separated complex fringe pattern.	21
Figure 4.3. An example of a scalogram with two local maxima related with two fringe families.	22

Figure 4.4. The photos of the specimen objects, which is produced via a 3-D printer.	23
Figure 4.5. An example of a non-deformed, square shaped fringe pattern.	25
Figure 4.6. Horizontal and vertical phase components of separated fringe pattern.	25
Figure 4.7. Wrapped phase maps of separated fringes.	26
Figure 4.8. Marked area that is used as a reference plane.	27
Figure 4.9. Captured and cropped flower shaped object.	27
Figure 4.10. Wrapped phase maps for the object.	28
Figure 4.11. Reference image for the flower shaped object.	28
Figure 4.12. Plot of the wrapped phase map for the reference image.	29
Figure 4.13. Topography for the flower shaped object after reference subtraction.	29
Figure 4.14. Topography of the image with fluctuated surface.	29
Figure 4.15. Captured and cropped image of an object with high steps.	30
Figure 4.16. 3D mesh plot of the object with steps.	30

LIST OF SYMBOLS

a	Scaling parameter of mother wavelet
b	Translation parameter of mother wavelet
I	Intensity of fringe signal
Im	Taking the imaginary part
J	Fourier transform of I
\mathcal{M}	Modulus array of \mathcal{W}
Re	Taking the real part
r_θ	Rotation parameter of mother wavelet
\mathcal{W}	Wavelet transform of a signal
ϕ	Height related phase distribution
Ψ	Fourier transform of ψ

LIST OF ACRONYMS/ABBREVIATIONS

1D	One Dimensional
2-D	Two Dimensional
3D & 3-D	Three Dimensional
CCD	Charged Couple Device
CWT	Continuous Wavelet Transform
FT	Fourier Transform

1.INTRODUCTION

The fringe projection method is commonly applied for reconstructing the topography of 3D objects since it has the advantages of being non-contact, precise and fast [1]. This method has two main application areas including industrial and medical ones. Optical metrology, corrosion analysis, refractive index measurements, roughness and strain measurements, topography of translucent objects and vibration and temperature sensing are considered as industrial application areas [2]. Examples for the latter can be given as scoliosis diagnosis, vascular wall deformation analysis, diagnosis of skin cancer [3].

The sinusoidal fringe pattern, which is projected onto a test object, is deformed depending on the height distribution of the object. This height distribution can be extracted by using a computational process on the deformed fringe pattern, such as Fourier transform (FT) [4], wavelet transform and phase shifting profilometry. After this process, unwrapped phase map is obtained between $-\pi$ and π . Required transition from unwrapped phase map to the wrapped map can be achieved by adding 2π or -2π to the certain parts of the unwrapped phase map [5]. However, this method becomes chaotic/insufficient when the test object is discontinuous or specular, which causes π phase jumps. The nature of sinusoidal fringes is altered on discontinuous objects, where the obtained unwrapped phase map is also discontinuous.

Our purpose is to quickly measure robust surfaces via a newly developed setup by using double beam splitters as a four-beam interferometer since they are compact and precise in measurements [6]. This arrangement has certain advantages. The most important one is that one can change the frequency of the fringes by rotating the beam splitters. This enables a great control over the fringe distributions. By applying multi-frequency fringes in two dimensions, the height distribution of the object is extracted in each dimension separately.

In this thesis, a new, sensitive and compact optical profilometric system is constructed in order to retrieve the 3D topography of an object. By utilizing double beam splitter system as a Gates' interferometer, the height distributions of various objects are extracted. Acquired images are processed by using 2-D continuous wavelet transform (2-D CWT). In later sections, this transformation 2-D CWT is discussed in detail.



2. REVIEW

2.1. Generation Methods for Square-Shaped Fringe Patterns

Young's double slit experiment is the pioneer of fringe pattern generation techniques which are widely used and are still in use in many fields [7]. The first study on retrieving the surface topography of an object was stated by Rowe and Welford in 1967 and new techniques are still developing today. In the following section, generation of square shaped fringe pattern method is summarized. An example of square - shaped pattern is shown in Figure 2.1.

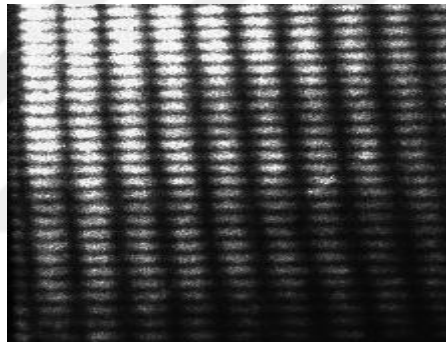


Figure 2.1: Square - shaped pattern that is captured by a charged couple camera (CCD) in a dark room.

2.1.1. Lloyd's Double Mirror Interferometer

Lloyd's arrangement utilizes a mirror and a single source to generate an interference pattern [8]. In Figure 2.2, there are two light beams. One of them comes directly from the source S and the other comes from the source S and reflected from the mirror, which can be considered as the imaginary source S'. The two beams interfere and form an interference pattern on the screen.

This arrangement is a resemble of Young's double slit experiment. The same arrangement can be used to form a square-shaped fringe pattern, which can be achieved by using, for example, double mirrors.

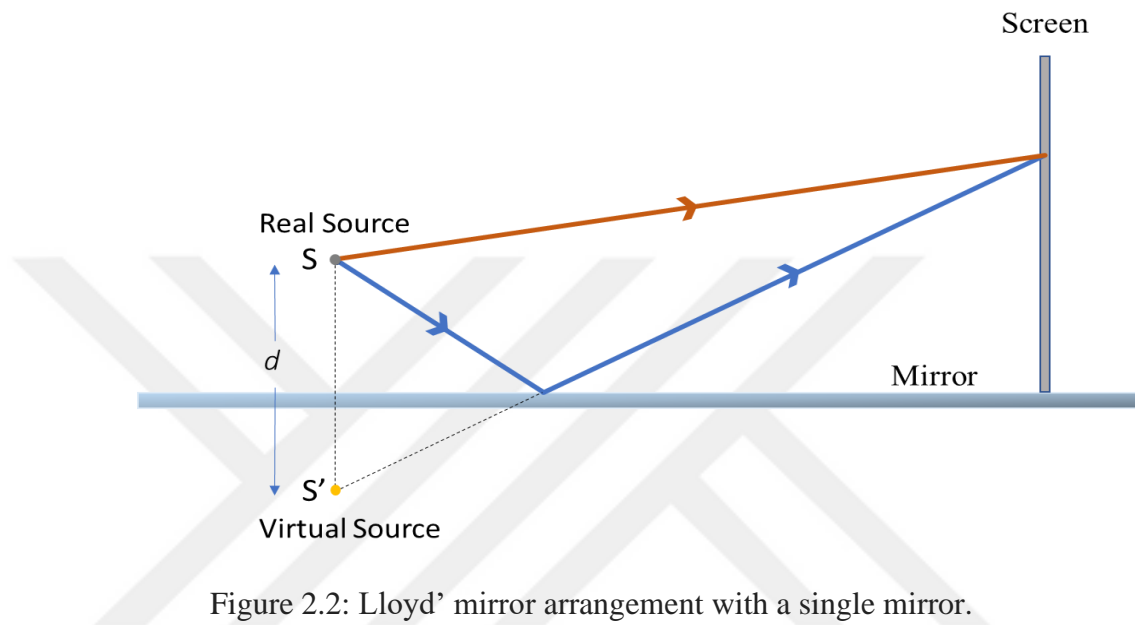


Figure 2.2: Lloyd' mirror arrangement with a single mirror.

In the setup shown in Figure 2.3, two mirrors accommodate perpendicular to each other, and there is an optical fiber as a single source (1) positioned between the mirrors. Therefore, virtual sources (2), (3) and (4) become new sources and the system seems to have four different sources for interference. The superposition of the electric fields of these sources generates square-shaped fringe patterns [9].

The system has a great advantage to change the fringe pattern distribution, which can be achieved by changing the distances between the source and the mirrors. The change in the distance is directly proportional to the fringe width, which results in an adjustable fringe frequency. In order to obtain fringe pattern with high frequency, the source fiber should be placed closer to the mirror plane. Another method for adjusting the frequency is rotating the mirror, which also changes the distances, and allows thinner or thicker fringes [10].

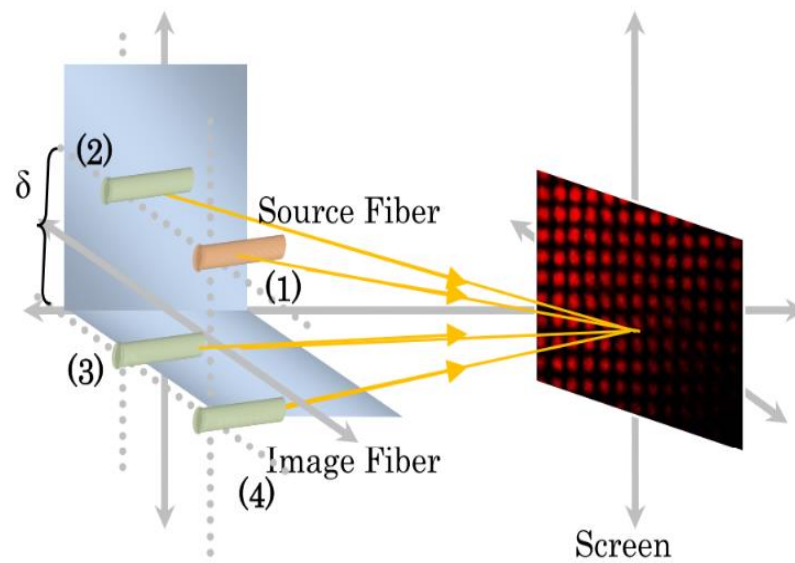


Figure 2.3. Lloyd's Double Mirror setup and interference of two fringe patterns by using four fiber sources [9].

2.1.2. Optical Fiber System

Optical fiber is a device which guides light with the phenomenon of total internal reflection. One of the application fields of optical fiber is generating fringe pattern for interferometric profilometry measurements with a high resolution and large dynamic range [11].

Yuan and *et al.* worked with single-mode polarization – maintaining three optical fibers as a source for fringe projection, which is shown in Figure 2.4. In this setup, changing the orientation of a fiber or a relative change in polarization angle by rotating the fiber around its axis result in generation of a square grid or hexagonal grid pattern, or a change in the visibility of the fringes. By using FT algorithm, topography is extracted from the modulated

pattern with the help of fusing the three phases or calculating the arithmetic mean of the phases [12].

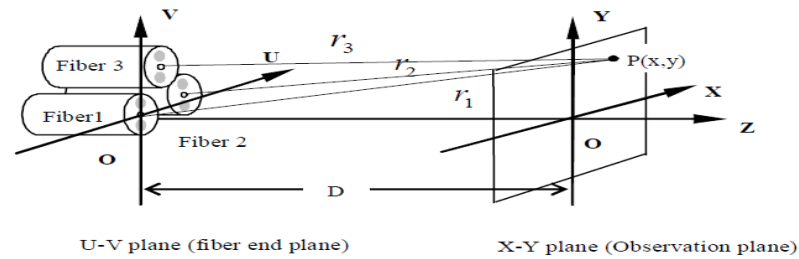


Figure 2.4. Three optical fiber system for fringe projection[12]

Another fringe projection method is using a four-core optical fiber. Each core can be regarded as a separate source. The combination of each couple of fibers results in different, two-dimensional fringe pattern. Vertical combination of the two cores generates horizontal fringes, and horizontal combination of the cores brings out vertical ones. Lastly, diagonal pairing of four cores in addition to the previous combinations generates square-shaped fringe patterns.

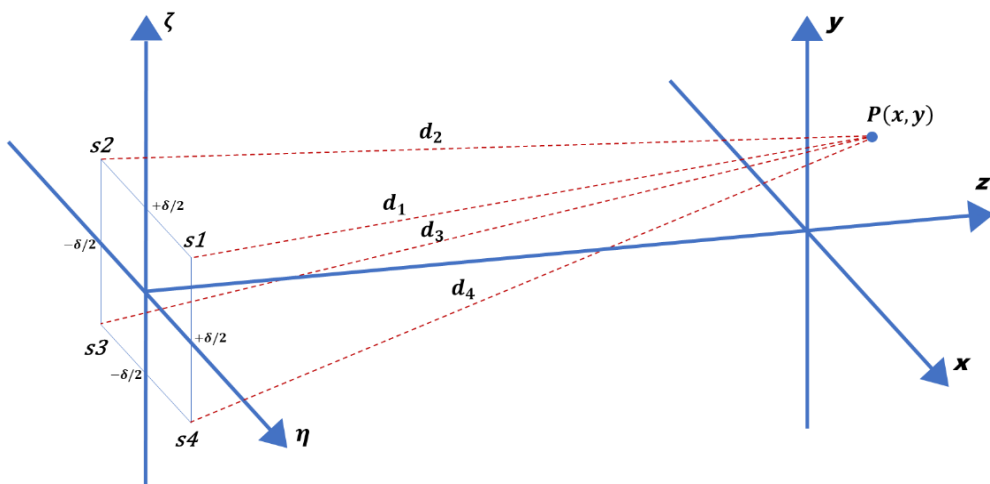


Figure 2.5. Formation of square shaped fringe pattern with four core optical fiber system.

In the wavelet transform analysis method, the shape of the deformed image is scanned horizontally and provides height distribution in the vertical axis for each shot.

In the case of having two-dimensional discontinuity in both vertical and horizontal axes, it is also needed to have vertical deformation, which can be achieved by a square-shaped fringe pattern. In the proposed method, this fringe is produced by using double beam splitter as a four-beam interferometer. In the following analysis part, electric field distribution of four beam interference will be derived.

Total electric field vector is the sum of the electric fields of each source:

$$\vec{E} = \vec{E}_1 + \vec{E}_2 + \vec{E}_3 + \vec{E}_4 \quad (2.1)$$

Intensity is proportional to the square of the time average of the magnitude of the electric field vector and its mathematical expression is as in Equation 2.2.

$$I = \langle \vec{E}^2 \rangle_T \quad (2.2)$$

$$I(x, y) = 2I_0 [2 + 2\cos(k(d_2 - d_1)) + 2\cos(k(d_3 - d_1)) + 2\cos(k(d_4 - d_1)) + 2\cos(k(d_3 - d_2)) + 2\cos(k(d_4 - d_2)) + 2\cos(k(d_4 - d_3))] \quad (2.3)$$

Two-dimensional intensity $I(x, y)$ can be expressed by the parameters d_1, d_2, d_3 and d_4 , which are the distances of each source to the target plane. Each distance can be computed by *Pythagorean theorem*:

$$d_i = [(x - n_i)^2 + (y - \zeta_i)^2 + z^2]^{1/2} \quad (2.4)$$

where i is an index and takes the values 1, 2, 3 and 4. By using Equation 2.4, equation for the distance can be written as

$$d_i = d \left[1 + \frac{\eta_i^2 + \zeta_i^2}{2d} - \frac{\eta_i x + \zeta_i y}{d} \right]^{1/2} \quad (2.5)$$

where $d = (x^2 + y^2 + z^2)^{1/2}$

For very large distance, we can use binomial approximation for Equation 2.5. Then, the distance equation becomes the following expression:

$$d_i = d + \frac{\eta_i^2 + \zeta_i^2}{2d} - \frac{\eta_i x + \zeta_i y}{d} \quad (2.5)$$

Then computation of each distance can be accomplished by using geometry according to Equation 2.6, and we substitute Equation 2.6 into Equation 2.3.

$$I(x, y) = 2I_0 \left[2 + 2 \cos \left(k \left(\frac{\delta x}{d} \right) \right) + 2 \cos \left(k \left(\frac{\delta y}{d} \right) \right) + \cos \left(k \left(\frac{\delta(x+y)}{d} \right) \right) + \cos \left(k \left(\frac{\delta(x-y)}{d} \right) \right) \right] \quad (2.6)$$

Where k is a propagation constant, which equals to $\frac{2\pi}{\lambda}$, and the phase dependent height is written as $z(x, y) = \frac{\lambda f}{2\pi \delta \sin \theta} \phi(x, y)$. Therefore, by using the phase dependent height, Equation 2.6 and geometrical properties in Figure 2.5, we get Equation 2.7, which is the intensity distribution of a four-point optical source captured by a camera.

$$I(x, y) = 2I_0 \left[2 + 2 \cos \left(2\pi \frac{\delta}{\lambda d} (x \cos \theta - z(x, y) \sin \theta) \right) + 2 \cos \left(2\pi \frac{\delta}{\lambda d} y \right) + \cos \left(2\pi \frac{\delta}{\lambda d} (x \cos \theta - z(x, y) \sin \theta + y) \right) + \cos \left(2\pi \frac{\delta}{\lambda d} (x \cos \theta - z(x, y) \sin \theta - y) \right) \right] \quad (2.7)$$

It is assumed that the intensity formula for a four-core interference in Equation 2.7 can be used for our experimental setup.

2.1.3. Moiré Pattern with Grating and Digital Fringe Projection

Moiré is a geometric pattern that is generated by the superposition of two or more straight or nonlinear lines. Basic moiré pattern, which is shown in Figure 2.6, includes one grid pattern and a second pattern with different fringe width, which is tilted α degrees with respect to the first interference pattern and overlaps with the other pattern. In order to get exact grid type pattern, two perpendicular binary or sinusoidal pattern should interfere with each other like in the last image of Figure 2.6.

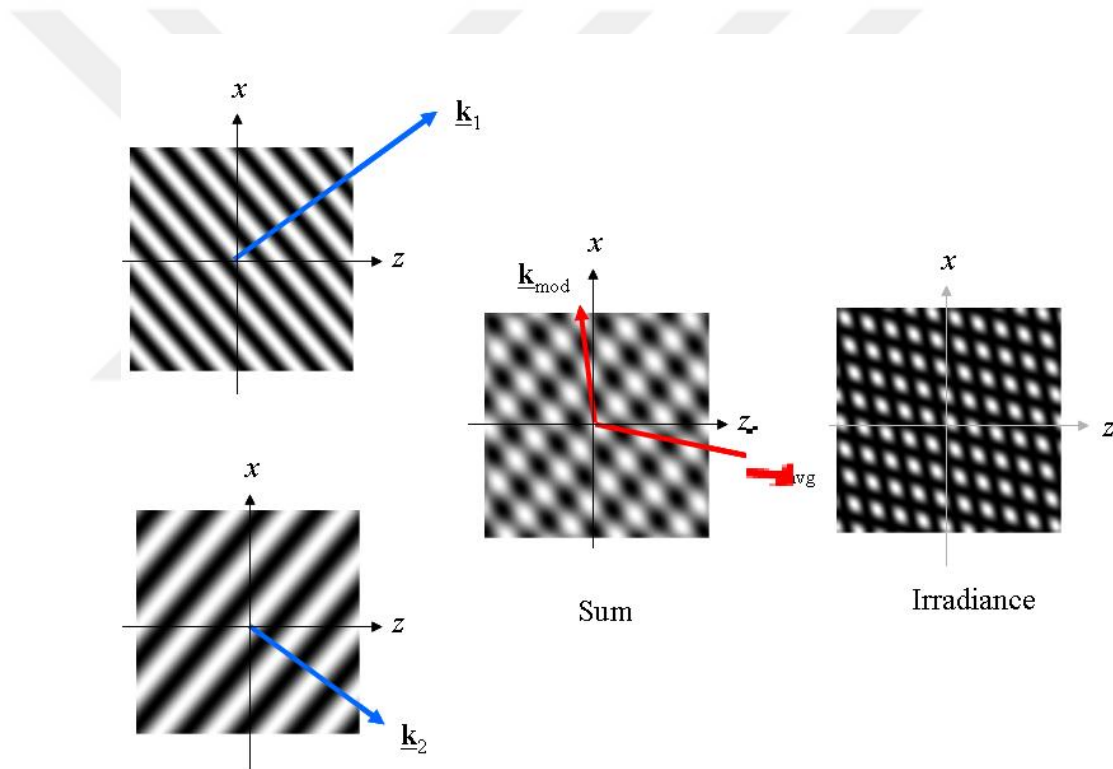


Figure 2.6. Moiré pattern generation [13].

The last method in this part is digital fringe projection profilometry. Several devices are used for obtaining a profilometry, and its scheme is shown in Figure 2.7 [14]. Digital fringe patterns are produced by a computer software. Fringe profile is directly linked to transmittance function. The fringe production is achieved by multiplying the transmission function with the intensity of light source and then the intensity of fringe distribution is

geometrically established. Then, a projector is used to transmit the pattern to a target object and deformation of the pattern is captured by a camera to be analyzed.

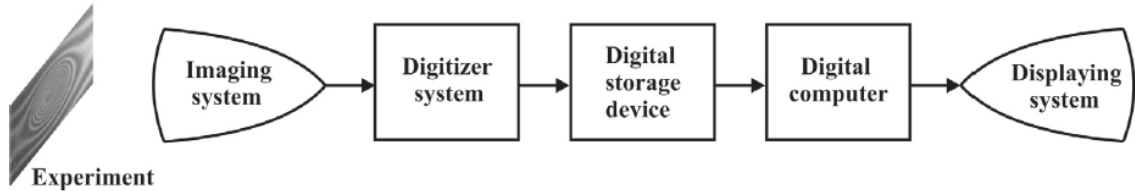


Figure 2.7. Scheme for a digital fringe pattern image processing system. [14].

Square-shaped fringe patterns can also be produced digitally by using a software. The relation of gratings can be mathematically expressed with multiplication of transmission functions of grating. The transmission function of sinusoidal line grating is following:

$$t = (1 + \cos(kx))/2$$

where k is a wave-vector and x is the coordinate axis. Multiplying two transmission functions results in one dimensional fringe pattern. Its three times multiplication with transmission function provides for square shaped fringe [15]. Various patterns can be generated in the same manner.

2.2. Analysis Method for Square-Shaped Fringe Pattern

2.2.1. Two-dimensional Continuous Wavelet Transform

2-D CWT and 1-D CWT are used in image processing, which have similar properties. However, 2-D continuous wavelet become popular on fringe pattern analysis since this analysis method has advantage of being accurate and automatic in noisy or complex fringe analysis [16]. 2-D CWT has also the ability to change and manipulate the shifting and scaling parameters [17]. In this section, the properties and the theory of 2-D CWT is studied.

Intensity of fringe signal can be written as in the following equation including the terms for both x and y components.

$$I(x, y) = I_0(x, y)[1 + V(x, y)\cos(2\pi f_0x + 2\pi f_0y + \phi(x, y))] \quad (2.8)$$

where $I_0(x, y)$ is background intensity, $V(x, y)$ is the visibility of the fringes. Spatial carrier frequency is f_0 , which should fulfil the following requirement to recover the phase.

$$2\pi f_0 > \left| \frac{d\phi(x)}{dx} \right|_{max} \quad (2.9)$$

2-D continuous wavelet transform is described as:

$$W(a, b, \theta) = \frac{1}{a} \int_{-\infty}^{\infty} I(x, y) \psi^* \left(\frac{x-b_x}{a}, \frac{y-b_y}{a}, r_\theta \right) dx dy \quad (2.10)$$

In Equation (2.10) $\psi^* \left(\frac{x-b_x}{a}, \frac{y-b_y}{a}, r_\theta \right)$ is called mother wavelet. There are three main geometric operations to perform the wavelet transform including scaling or dilation, rotation, translation. $a(a > 0)$ is the scaling parameter, $b \in R^2$ is the translation parameter, and the rotation parameter has the following expression:

$$r_\theta = \begin{pmatrix} \cos \theta & -\sin \theta \\ \sin \theta & \cos \theta \end{pmatrix}$$

where θ is a rotation angle, which has a range between 0 to 2π .

Whole pixels are processed with the wavelet transformation. The mother wavelet is rotated with r_θ and also shifted in the x and y direction with the parameter b_x and b_y while

it is scaled with the parameter a on the fringes in every iteration of the code. Certain essential mathematical requirements must be satisfied to consider a function as a mother wavelet [18].

- The image signal $I(x)$ can be reproduced from its wavelet transform $J(a,b,\theta)$ by the reconstruction formula:

$$I(x) = \frac{1}{c_\psi} \iint_{\mathcal{R}^2} d^2b \int_0^\infty \frac{da}{a^3} \int_0^{2\pi} d\theta J(b, \theta, a) \psi_{b,\theta,a}(x) \quad (2.11)$$

where c_ψ is admissibility constant, and the admissibility condition is given in Equation 2.12 which should be satisfied by the two-dimensional wavelet transform and $\psi \in \mathcal{L}^2(\mathcal{R}^2, d^2x)$

$$c_\psi = (2\pi)^2 \int_0^\infty \frac{|\Psi(f)|^2}{f^2} d^2f < \infty \quad (2.12)$$

- This condition implies that the wavelet has zero mean:

$$\int_{-\infty}^\infty \psi(x) dx^2 = 0 \quad (2.13)$$

- 2-D signal should have finite energy where $I \in \mathcal{L}^2(\mathcal{R}^2, d^2x)$:

$$\iint_{\mathcal{R}^2} |I(x)|^2 d_x^2 < \infty \quad (2.14)$$

Wavelet transform conserves the norm of the fringe signal. Thus, its total energy forms a resolution of the identity:

$$\iint_{\mathcal{R}^2} |I(x)|^2 d_x^2 = \frac{1}{c_\psi} \iint_{\mathcal{R}^2} d^2b \int_0^\infty \frac{da}{a^3} \int_0^{2\pi} d\theta |J(b, \theta, a)|^2 \quad (2.15)$$

which generates a resolution of the identity:

$$J = \frac{1}{c_\psi} \iint_{\mathbb{R}^2} d^2b \int_0^\infty \frac{da}{a^3} \int_0^{2\pi} d\theta |\psi_{b,\theta,a}\rangle \langle \psi_{b,\theta,a}| \quad (2.16)$$

From the resolution identity, the following can be derived

$$\begin{aligned} & \iiint_G d^2b \frac{da}{a^3} d\theta |J(\vec{b}, a, \theta)|^2 = \\ & = \int_{\mathbb{R}^2} d^2\vec{k} \int_{\mathbb{R}^2} d^2\vec{k}' \iiint_G d^2b \frac{da}{a^3} d\theta \times e^{i\vec{b}\cdot(\vec{k}-\vec{k}')} \overline{\Psi(ar_{-\theta}(\vec{k}))} \Psi(ar_{-\theta}(\vec{k}')) J(\vec{k}) \overline{J(\vec{k}')} \\ & = (2\pi)^2 \int_{\mathbb{R}^2} d^2\vec{k} \int_0^\infty \frac{da}{a} \int_0^{2\pi} d\theta |\Psi(ar_{-\theta}(\vec{k}))|^2 |J(\vec{k})|^2 \\ & \int_0^\infty \frac{da}{a} \int_0^{2\pi} d\theta |\Psi(ar_{-\theta}(\vec{k}))|^2 = \int_0^\infty \frac{d\rho}{\rho} \int_0^{2\pi} d\theta |\Psi_p(\rho, \phi - \theta)|^2 \\ & = \int_0^\infty \frac{d\rho'}{\rho'} \int_0^{2\pi} d\theta' |\hat{\psi}_p(\rho', \theta')|^2 \\ & = \int_{\mathbb{R}^2} \frac{d^2\vec{k}'}{|\vec{k}'|^2} |\hat{\psi}(\vec{k}')|^2. \end{aligned}$$

Where magnitude of the vector \vec{k} is equal to ρ , and $\Psi_p(\rho', \theta')$ is the polar coordinate form of $\Psi(\vec{k}')$

$$= \int_{\mathbb{R}^2} \frac{d^2\vec{k}'}{|\vec{k}'|^2} |\Psi(\vec{k}')|^2$$

2-D CWT can be written as a its general integral form in general:

$$\mathcal{W}(a; b; \theta) = a \int_{-\infty}^{\infty} \int_{-\infty}^{\infty} \Psi^*(ar_{-\theta}\alpha_x, ar_{-\theta}\alpha_y) \mathcal{J}(\alpha_x, \alpha_y) \quad (2.17)$$

The selection of mother wavelet is significant for fringe analysis, and some examples of mother wavelets in two dimensions are *Halo* and *Arc*, *Morlet*, *Mexican hat*, *Cauchy* and *Poisson* wavelets. *Morlet* wavelet as mother wavelet is chosen in this study whose definition is as follows:

$$\psi\left(\frac{x-b_x}{a}, \frac{y-b_y}{a}, r_\theta\right) = e^{i\left(\frac{(x-b_x)\cos\theta + (y-b_y)\sin\theta}{a}\right)} e^{-\left(\frac{(x-b_x)^2 + (y-b_y)^2}{2a}\right)} \quad (2.18)$$

Firstly, Fourier transformations of the mother wavelet and the fringe intensity are taken, which are indicated with the letters Ψ and \mathcal{J} respectively. The symbol “ * ” denotes the complex conjugate.

$$\Psi(ar_{-\theta}\alpha_x, ar_{-\theta}\alpha_y) = e^{-\left(\frac{(a\alpha_x - c\cos\theta)^2 + (a\alpha_y - c\sin\theta)^2}{2}\right)} \quad (2.19)$$

where Equation 2.19 shows FT of Morlet wavelet, and this integral will be evaluated by the *convolution theorem* with new variables α_x and α_y . Then, the following equation explains FT of the signal:

$$\mathcal{J}(\alpha_x, \alpha_y) = \mathcal{K}_1 + \mathcal{K}_2 + \mathcal{K}_3 \quad (2.20)$$

$$\mathcal{K}_1 = 2\pi I_0(b_x, b_y) \delta(\alpha_x, \alpha_y)$$

$$\mathcal{K}_2 = \pi I_0(b_x, b_y) V(b_x, b_y) e^{i(\phi_b - b_x\phi'_x - b_y\phi'_y)} \delta(\alpha_x - 2\pi f_0 - \phi'_x, \alpha_y - 2\pi f_0 - \phi'_y)$$

$$\mathcal{K}_3 = \pi I_0(b_x, b_y) V(b_x, b_y) e^{-i(\phi_b - b_x\phi'_x - b_y\phi'_y)} \delta(\alpha_x - 2\pi f_0 - \phi'_x, \alpha_y - 2\pi f_0 - \phi'_y)$$

where $\phi_b = \phi(b_x, b_y)$, $\phi'_x = \partial\phi(b_x, b_y)/\partial x$ and $\phi'_y = \partial\phi(b_x, b_y)/\partial y$. These parameters are defined by approximating fringe phase which depends on the localization property of 2-D CWT [19]

The last expression (2.21) is CWT for Morlet wavelet with the parameters a , b_x , b_y , and angle θ , which means that this equation is a four-dimensional matrix of complex wavelet coefficients and it is hard to visualize [20]:

$$\begin{aligned} \mathcal{W}(a; b_x; b_y; \theta) &= \pi I_0(b_x, b_y) V(b_x, b_y) e^{i(\phi_b + 2\pi f_0 b_x + 2\pi f_0 b_y)} \\ &\times e^{-\frac{1}{2}((2\pi f_0 + a\phi'_x - c \cos \theta)^2 + (2\pi f_0 + a\phi'_y - c \sin \theta)^2)} \end{aligned} \quad (2.21)$$

Modulus is magnitude of the wavelet coefficient, which can be calculated by the formula:

$$\mathcal{M}(a; b_x; b_y; \theta) = \sqrt{\text{Im}[\mathcal{W}(a; b_x; b_y; \theta)]^2 + \text{Re}[\mathcal{W}(a; b_x; b_y; \theta)]^2} \quad (2.22)$$

We can consider on this critical point. Modulus becomes maximum when the two condition is satisfied at the same time. The first one is that frequency of the daughter wavelet is adjacent to the fringe pattern frequency, and second one is that rotation of mother wavelet has the similar orientation of the fringes. For corresponding conditions, modulus of wavelet $\mathcal{W}(a; b_x; b_y; \theta)$ reaches its maximum value, and generates ridge function $\mathcal{W}_r(a_r; b_x; b_y; \theta)$ where the scale parameter a_r is called ridge point [21].

Then the phase of the signal is obtained as follows:

$$\mathcal{P}(a_r; b_x; b_y; \theta) = \tan^{-1} \left(\frac{\text{Im}[\mathcal{W}_r(a_r; b_x; b_y; \theta)]}{\text{Re}[\mathcal{W}_r(a_r; b_x; b_y; \theta)]} \right) \quad (2.23)$$

This is wrapped phase that ranges between $-\pi$ and π so unwrapping procedure is required to get the phase, which includes real height information. Since the shifting parameter b is directly related with x and y components, unwrapped phase can be written as:

$$\mathcal{P}(x, y) = \tan^{-1} \left(\frac{\text{Im}[\mathcal{W}_r(a_r; b_x; b_y; \theta)]}{\text{Re}[\mathcal{W}_r(a_r; b_x; b_y; \theta)]} \right) \quad (2.12)$$



3. EXPERIMENTAL

3.1. Setup

The main component of the fringe projection system is the fringe production process, which is provided by a source (He-Ne) laser of 632.8 nm wavelength in this study. Laser light is expanded about 10 times via optical plano-convex collimating lenses and pass through two beam splitters. The optical system is called the Gates interferometers [22]. Firstly, expanded and collimated laser beam goes through the diagonal of a cubic beam splitter, which means that the cubic beam splitter is rotated exactly by 45 degrees with respect to the wave front of the laser rays, then an equal portion of the laser beam is separated into two planes which form a sinusoidal projected fringe pattern [23]. The experimental setup is shown in Figure 3.1. Micrometer stage is used to shift the object on a surface, then empty area with fringe patterns is captured to use as a reference image.

In order to get a square-pattern and two-dimensional information from the object, the second cubic beam splitter is rotated by 90 degrees with respect to the first beam splitter. While the first cube generates fringes in y-direction, the second cube generates fringes, which is also rotated as the second cube, in x-direction. Fields of the two perpendicular patterns superpose with each other to generate the square-shaped pattern, which is theoretically similar to four core interferences system in [24]. The images are captured by CCD camera, which is oriented at 90 degrees with respect to the reference plane. A photograph of the pattern is taken by a CCD camera and is turned into a digital signal. These signals are gathered and analyzed by a personal computer for the fringe processing with the aid of MATLAB.

To analyze height distribution of a discontinuous object, each region with discontinuous height are cropped from the image and topographies of these discontinuous heights are obtained by using 2-D continues wavelet transform. After the analysis, every topography is combined to reconstruct the total shape of the object.

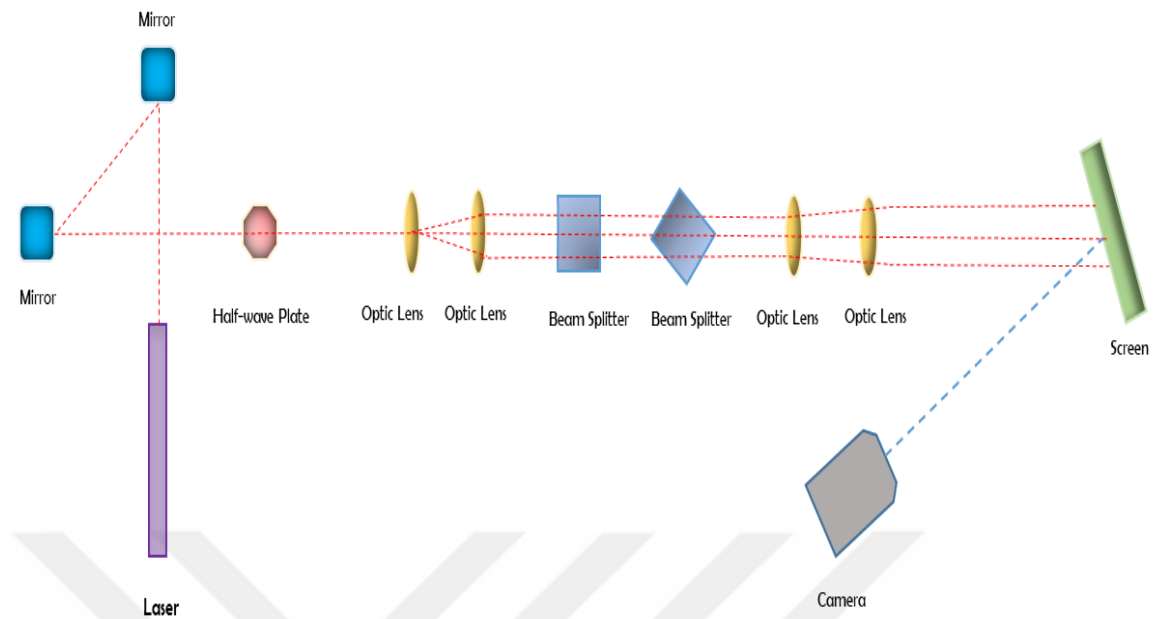


Figure 3.1. Sketch of our experimental setup.

3.2. Gates' Interferometry and Double Beam-Splitter

A beam splitter is an object used commonly to construct an interferometric setup, such as *Michelson Interferometer*, *Linnie interferometer*, *Spectral interferometry* etc. When a light beam is incident on a less dense medium with an angle, which is greater than the critical angle, it is expected to observe a total internal reflection. If the thickness of the less dense medium is crucially decreased, the incident light partially escapes to the forbidden regions and is transmitted into the medium after the less dense one. This phenomenon is called the optical tunneling [25].

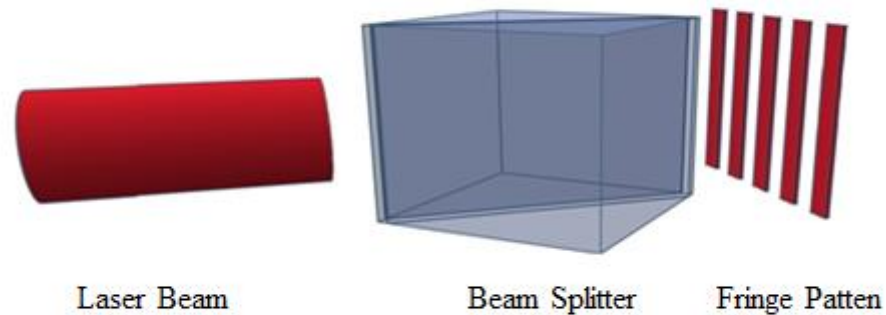


Figure 3.2. *Gates' interferometer* was sketched by CAD design tool, Tinkercad .

A famous example of this phenomenon is observed in a beam splitter, which consists of two biprisms and a thin film between with a lower refractive index than the biprisms [26]. By utilizing this principle, Köster used two biprisms to generate a fringe pattern in 1995 [27]. Then Gates arranged Köster's prisms and used beam splitter itself as a fringe pattern generator, which enables to design compact, simple and sensitive setup by using it as an optical interferometry [28-30]. The main advantage of the Gate' Interferometer is creating two interferometers with relatively π phase shift difference

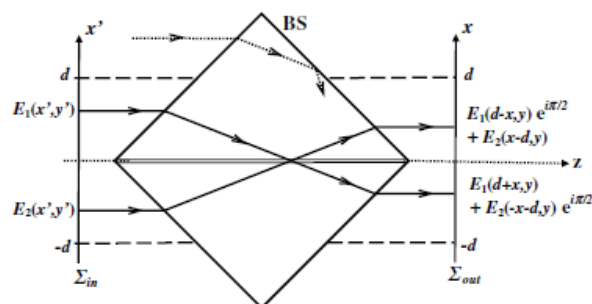


Figure 3.3. Gates' interferometer shows transmission and reflection of incident rays [30].

Each beam splitter is placed such that the incoming laser beam splits into two beams with equal intensity and symmetric shape Each transmission of light generates a fringe pattern since the transmission of the cube. In order to get the square pattern and two-

dimensional information from the object surface, the second beam splitter is rotated 90 degrees around the axis of the beam propagation.

Therefore, the second fringe pattern is also rotated with the cube and superposes with the other pattern as seen in Figure 3.4. The greatest advantage of using beam splitters is that they enable one to control fringe frequency precisely since the rotation of the cubic beam splitters change the fringe frequency [30].

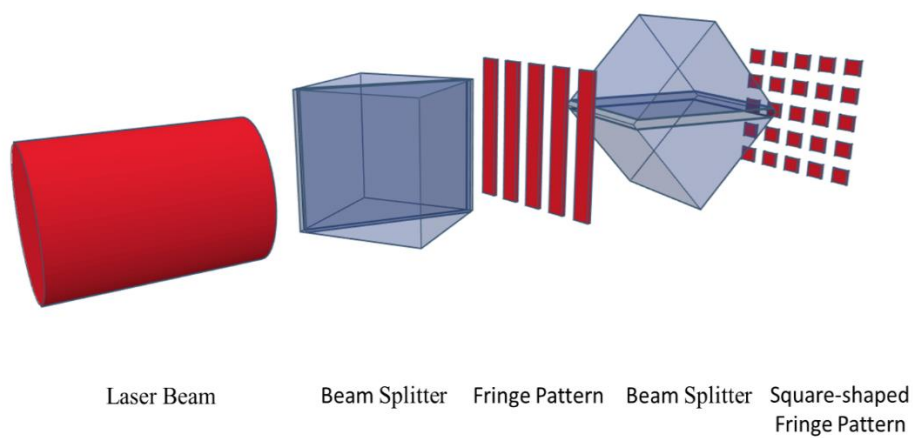


Figure 3.4. Double beam splitter arrangement for interferometric measurements.

4. ANALYSIS

4.1. Algorithm to Separate Fringe Patterns

2-D CWT hinges on techniques that are constructed to demodulate fringes in a single image. However, this image may include complex or two-dimensional fringe patterns so as to enhance the quality of the topographies of objects. It is possible to extract some specific information from a given fringe family in the related dimension. In the case of analyzing discontinuous heights, this is achieved by separating overlapped fringes by a separation code using 2-D CWT [31]. The idea behind the separation algorithm is ridge extraction. Ridge function is directly related to the fringe family as it is modulus maxima.

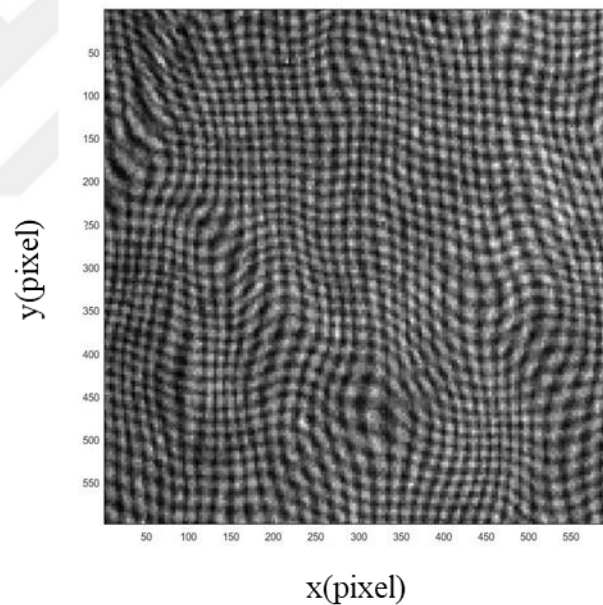


Figure 4.1. A complex fringe pattern [31].

Figure 4.1 shows complex moiré type fringe pattern to be tested by the fringe separation algorithm. This fringe is separated into horizontal and vertical components as seen in Figure 4.2.a and 4.2.b, respectively.

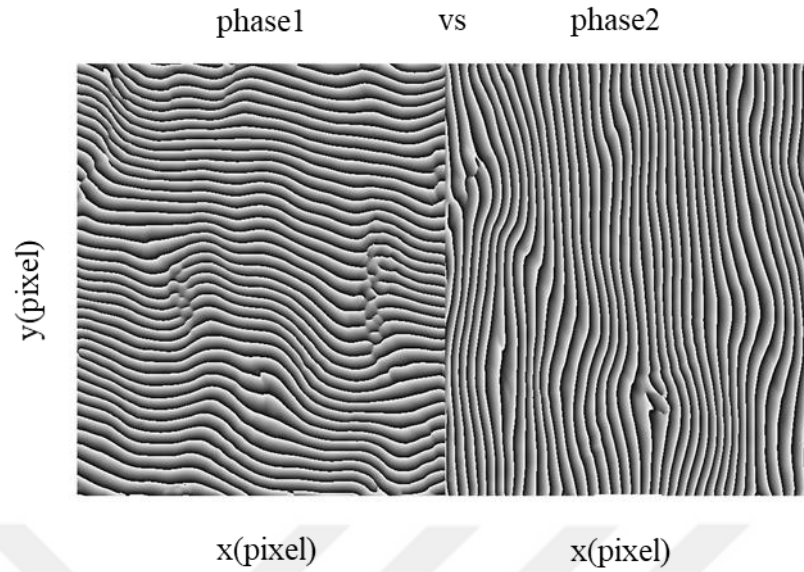


Figure 4.2.a and 4.2.b: Horizontal and vertical phase components of separated complex fringe pattern.

4.1.1. Ridge Extraction & Construction of a Reliability Map

There are crucial steps to follow in order to split the fringe patterns into two families. Firstly, wavelet transform of signal is taken to obtain $\mathcal{W}(a; b_x; b_y; \theta)$ modulus, which is the amplitude of the complex array, and it is calculated for each pixel using the formula 2.22. Then, modulus is constructed as a function of wavelet coefficients, namely the scale parameter a and angle θ , which is called a scalogram and is a two-dimensional matrix shown in Figure 4.3.

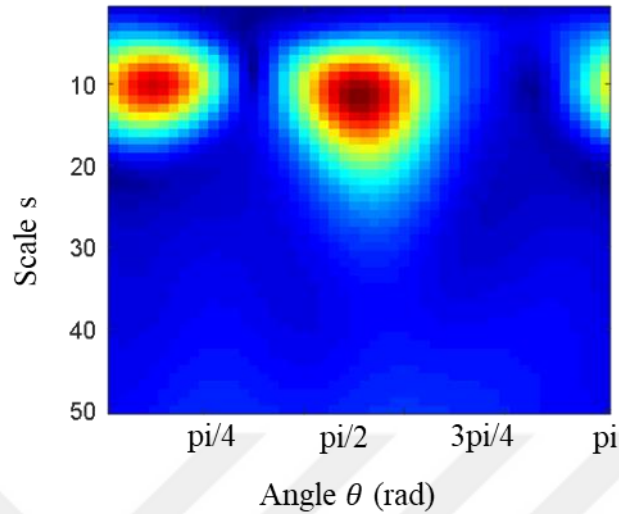


Figure 4.3. An example of a scalogram with two local maxima related with two fringe families.

If one fringe family exists, it is possible to see one peak in the scalogram. However, some maxima are divided due to splitting of the peaks, which are regarded as virtual in the scalogram. The virtual peak belongs to half part of a local maxima peak. In order to eliminate this problem and merge the peak distribution, it is required to cut and translate the map by $\frac{\pi}{2}$ rad in the angle axis. Then, the shortest distance between peaks is compared and selected, and a new map is generated with these values by placing them into the exact pixel position in the real map. The new formed map is called reliability map.

Several local maxima can appear as parasitic maxima in the scalogram, which should be eradicated. The highest reliability value in the map should be detected to generate ridge map construction. Starting from this maximum value, one local maxima in the scalogram is randomly chosen. Its complex value of wavelet coefficient is accumulated as a gain, and one of the adjacent four pixel with the highest reliability value goes through to the same procedure and this procedure is repeated for neighboring pixels.

A two-dimensional CWT is used to analyze deformed square shaped fringes. Two specimen objects are tested by utilizing double beam splitter arrangement. Second object has discontinuous steps, which have 2 dimensional discontinuities in vertical and horizontal axes.

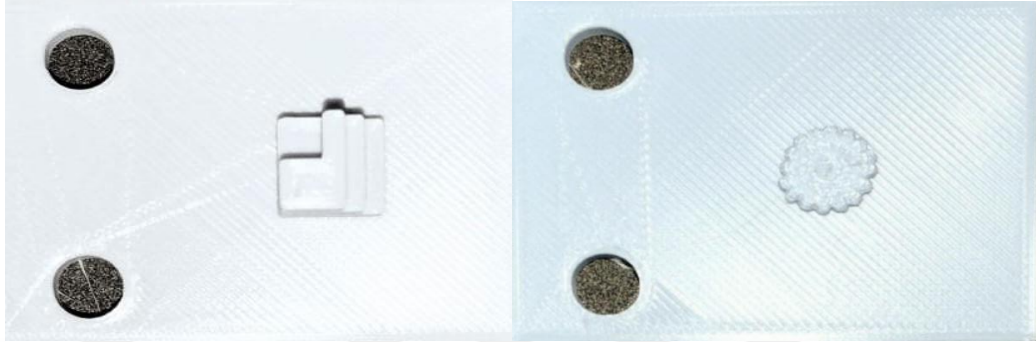


Figure 4.4. The photos of the specimen objects, which are produced via a 3-D printer.

Vertical fringes are used to analyze horizontal steps as shown in Figure 4.2 and the horizontal fringes are utilized to eliminate higher step ambiguity on the vertical steps.

4.1.2. Phase Unwrapping Procedure

Because of the nature of arctangent function, obtained phase map ranges between $-\pi$ and π values. Therefore, the right-hand side of the Equation 4.1, which is mentioned before in 2-D CWT part, is needed to be unwrapped.

$$\mathcal{P}(x, y) = \tan^{-1} \left(\frac{\text{Im}[\mathcal{W}(a; b_x; b_y; \theta)]}{\text{Re}[\mathcal{W}(a; b_x; b_y; \theta)]} \right) \quad 4.1$$

$$\mathcal{P}(x, y) = \tan^{-1} \left(\frac{\text{Im}[\mathcal{W}(a; b_x; b_y; \theta)]}{\text{Re}[\mathcal{W}(a; b_x; b_y; \theta)]} \right) = 2\pi f_0 x + 2\pi f_0 y + \phi(x, y) \quad 4.2$$

Wrapped map includes two terms in Equation 4.2. One of them is $2\pi f_0$, where f_0 is the carrier frequency, and the other one is the term $\phi(x, y)$, which is the phase term related with the real height distribution. After the unwrapping process, the term $2\pi f_0$ should be removed to obtain the height distribution. This unwrapping process is executed by means of personal computer. Deformed fringe signal is captured by a CCD camera and converted into digital signal. FT of every row of the image signal is taken and then insert in 2-D CWT algorithm in MATLAB [32]. Thus, Fourier transformed 2-D signal and Fourier transformed 2-D wavelet is multiplied and the integral of this multiplication is taken with the parameters a , b , and θ , which is processed like in Equation 2.8. By using maxima of scaling factor a_r , wavelet ridge function is calculated by ridge point. After this step, separation algorithm is applied which is mentioned in the previous part. Then, we have two wrapped phases. MATLAB codes used in the study are [33] and [34], which are applied to unwrapped phases, and $2\pi f_0 x + 2\pi f_0 y + \phi(x, y)$ is collectible.

A sample non-deformed fringe pattern is demonstrated in Figure 4.5, and it is analyzed and separated into two components as phase1 and phase2, respectively as seen in Figure 4.6. Then, the wrapped phases corresponding to these phases are obtained as seen in Figure 4.7.

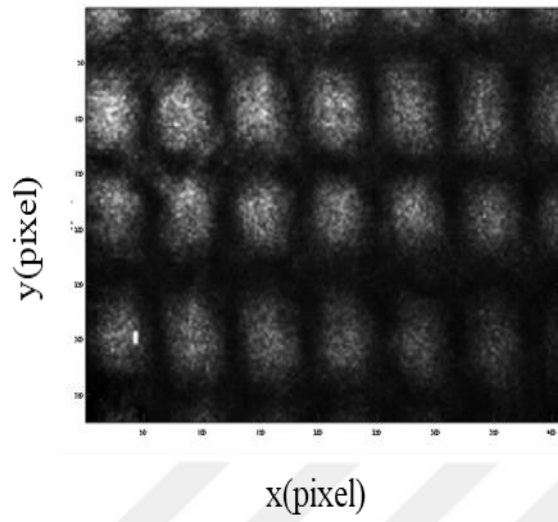


Figure 4.5. An example of a non-deformed, square shaped fringe pattern.

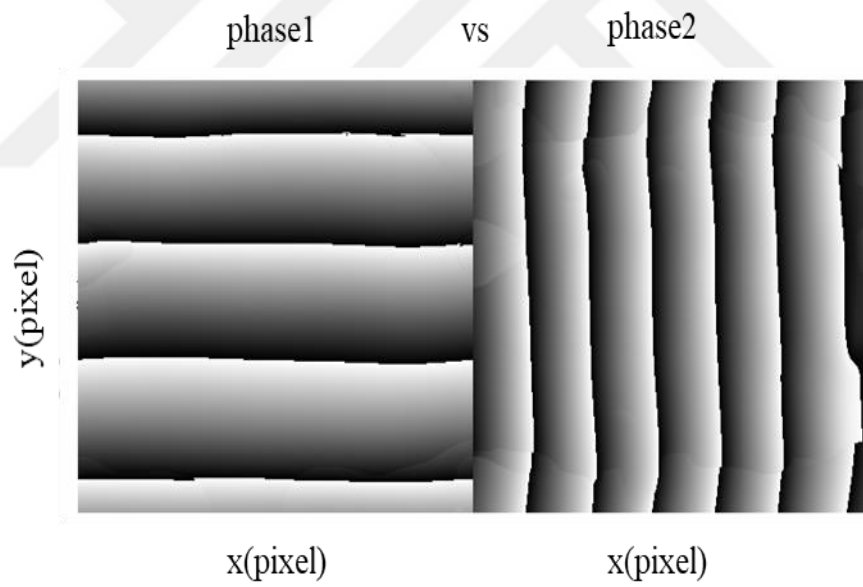


Figure 4.6. Horizontal and vertical phase components of separated fringe pattern.

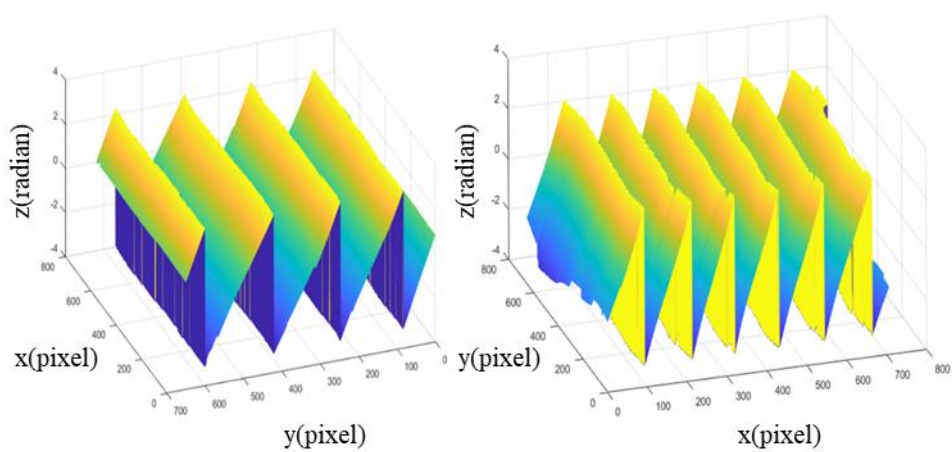


Figure 4.7. Wrapped phase maps of separated fringes.

4.1.3. Removing Carrier Frequency

After obtaining the unwrapped phase, the process to acquire the exact height distribution starts with removing $2\pi f_0$. Then, continues with extracting the phase $\phi(x, y)$, which is related to the object height. Reference image is used to remove the term $2\pi f_0$. f_0 is a constant directly related to the spatial frequency of the produced fringe pattern. An example of a reference image is demonstrated in Figure 4.11. The objects are positioned with the help of a micrometer stage, which provides movement in every direction for the object. Object shifted to x axis and empty space is filled by non-deformed fringe pattern, which is reference image. We captured the image of the reference plane, and the same algorithm is applied, and wrapped phase of the reference is illustrated in Figure 4.12.

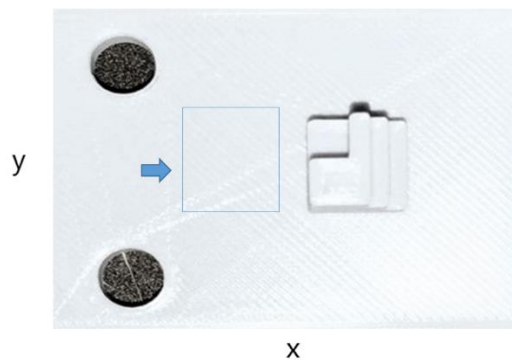


Figure 4.8. Marked area that is used as a reference plane.

4.2. Results and Discussion

4.2.1. Flower Shaped Object

The images are captured and processed with the aforementioned algorithm. Due to the illumination angle, shadows appear on the captured image, which result in holes in the obtained topography. One should be careful about the shadows and try to eliminate them as much as possible. The captured image for the object is seen in Figure 4.9.

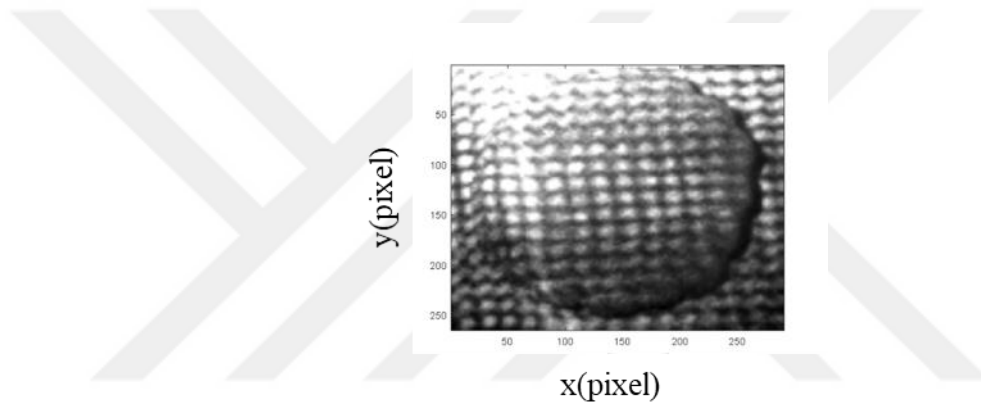
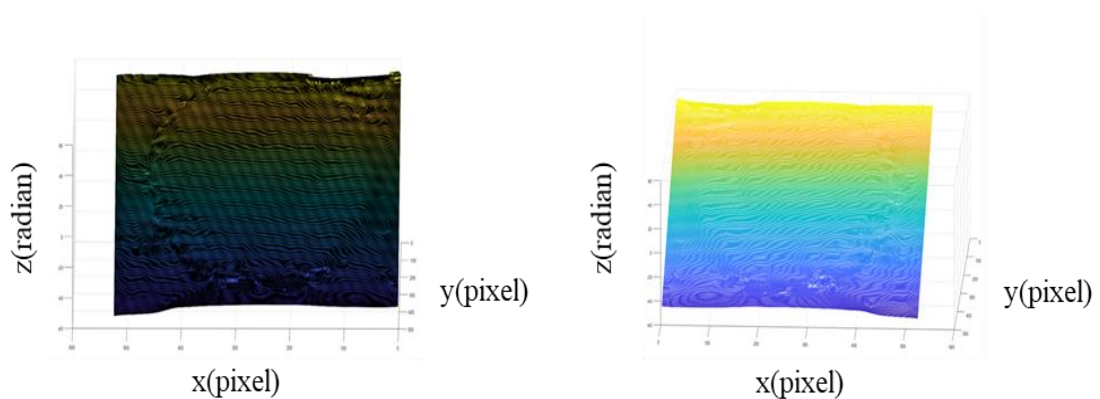


Figure 4.9. Captured and cropped flower shaped object.



4.10.a Surface plot of the unwrapped phase map 4.10.b Mesh plot of the unwrapped phase map.

Figure 4.10. Unwrapped phase maps for the object.

Wrapped phase map of the object is shown in Figure 4.10 with two different plotting. The same procedure is applied on the reference image. Then, MATLAB unwrapping code

is applied for these two images. To generate the exact topography of the object, unwrapped phase map of the reference image seen in Figure 4.11 should be mathematically subtracted from the unwrapped phase map of the object in Figure 4.10. The subtracted phase map to get the topography as demonstrated in Figure 4.13.

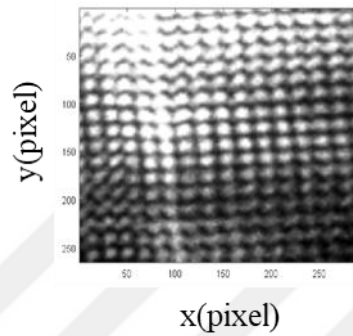


Figure 4.11. Reference image for the flower shaped object.

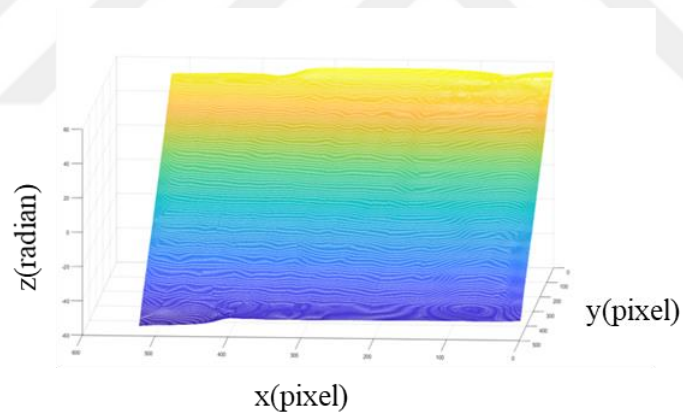


Figure 4.12. Plot of the unwrapped phase map for the reference image.

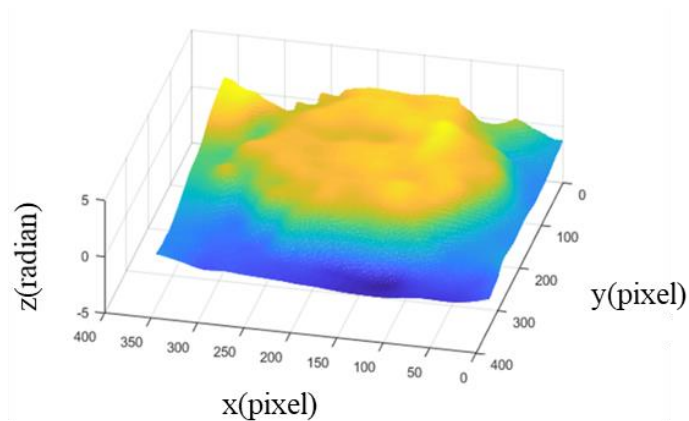


Figure 4.13. Topography for the flower shaped object after reference subtraction.

The fluctuations seen in the topography in Figure 4.14 stem from the error of the code. In order to get rid of the extra fluctuations, the size of the image is enlarged twice before and after the denoising process.

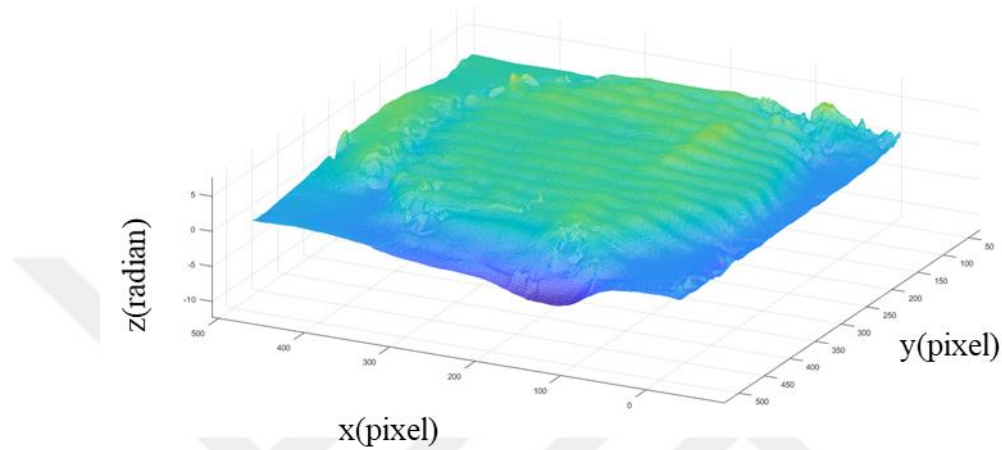


Figure 4.14. Topography of the image with fluctuated surface.

4.2.2. Object with Steps

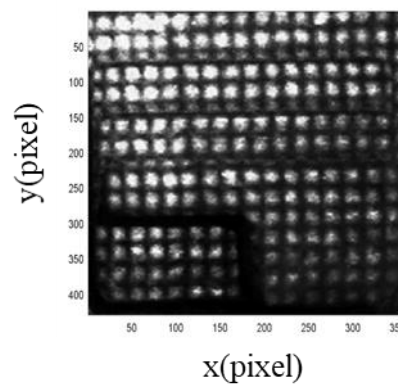


Figure 4.15. Captured and cropped image of an object with high steps.

In Figure 4.15, cropped and denoised object with high steps is shown. The same procedure as before is applied here too. Since heights of the steps are not equal, the number of fringes on a single step in x any y directions are variously chosen, which are 13 and 15,

respectively. This is achieved by rotating beam-splitter cubes. The topography of the object with steps is shown in Figure 4.16.

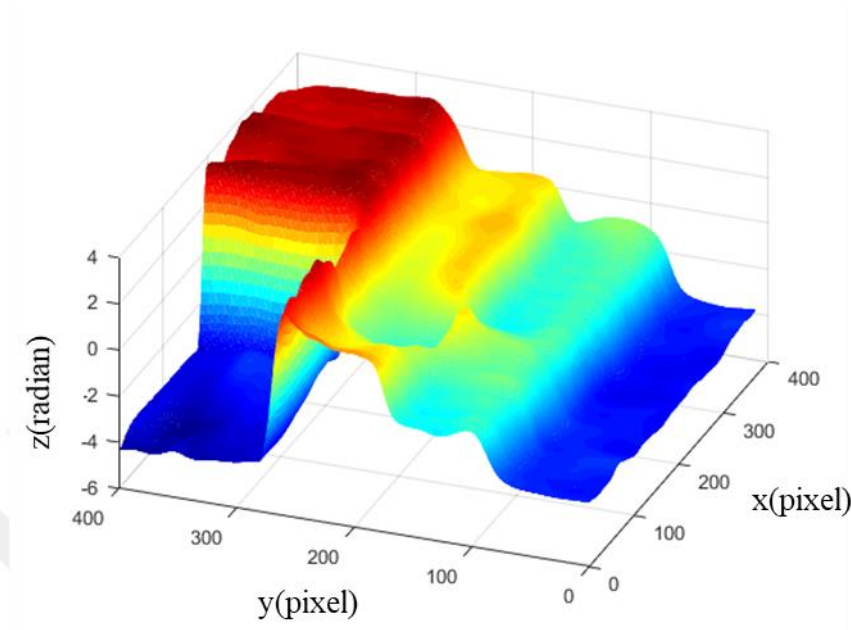


Figure 4.16. 3D mesh plot of the object with steps.

As justified above, the interference pattern is easily produced by using a double beam splitter configuration, which is basically a four-beam interferometer, where a HeNe laser is utilized as the light source. It is crucial to transmit the beam almost equally to the two sides of the beam splitter cubes. In this way, equally distributed fringe pattern is obtainable. Due to the two cubic beam splitters in the experimental setup, we get 4 divided and symmetrical fringes, which have enough visibility. Therefore, using one portion of these pattern is enough for conducting the experiments. The system is compact and simple when compared to a digital fringe projection system or a four-core fiber configuration. Therefore, there is no need to any external manufacturing process like an additional projection unit.

In this experimental setup, beam splitters are fixed onto multi axes stages to control the angle of the cubes with respect to the incoming beam and consequently the fringe frequencies on the screen. It is seen that this system is highly sensitive to the rotations. This aspect is the outstanding feature of the experimental setup. Depending on the complexity or roughness of the object, one can use the proposed setup to produce thinner or thicker fringes in a short interval of time. Thinner fringes are capable of extracting the details of an object, while thicker fringes are useful to extract information from rough object surfaces. Most

importantly, these are achievable separately on two perpendicular fringe patterns at the same time.

In the topography of the object with discontinuous steps, deteriorations can be seen. The root of this problem is the shadows at the edge of the steps and resolution deficit. Resolution of images is not adequate to carry all information. As a result of this, deformations are seen in the Figure 4.16. In the future work, topographies can be enhanced by capturing high resolution images. Also, phase should be calibrated to get the height distribution, because the deepest step in the object looks like it is on the same level as the reference plane. However, the phase value deviates from its real height.

By its nature, beam splitter causes an extra fringe pattern with fixed frequency. This can be also a source of an error for height distribution, because the extra pattern makes fringe separation difficult [31]. In a future work, eliminating these additional fringes is also considered. Last but not least, surface of the objects illustrated in Figure 4.4 has slightly shiny regions in its distribution. This can also be a source of error.

In this study, images are captured with Optronis Cr600×2 CCD camera at 256× 256 resolution. These images are analyzed using the software MATLAB and version 2017b. The object is designed in the online 3D design tool Tinkercad and produced with a 3D printer.

5. CONCLUSION

In this thesis, it is demonstrated that a new setup is developed by using a double beam splitter configuration for fringe projection system, which is inspired from Gates's interferometer. The setup accomplishes extraction of height distributions of various non-specular objects. The main advantage of this system is that it has the ability to adjust fringe pattern distribution to get a higher quality topography of the objects.

For the analysis part, two dimensional continues wavelet with morlet mother wavelet is mainly explained for separating two fringe families and is demonstrated that it is quite adequate to extract the topography of various objects.

REFERENCES

1. Xu, Y., “Uniaxial three-dimensional shape measurement with projector defocusing.”, *Optical Engineering*, 51(2), p. 023604, doi:10.1117/1.oe.51.2.023604, 2012.
2. Xu, Y., H. Zhao, H. Jiang, and X. Li, “High-accuracy 3D shape measurement of translucent objects by fringe projection profilometry.”, *Optics Express*, 27(13), pp. 18421-18434, doi:10.1364/oe.27.018421, 2019.
3. Rey-Barroso, L., F. J. Burgos-Fernández, M. Ares, S. Royo, S. Puig, J. Malvehy, G. Pellacani, D. Esipnar, N. Sicilia, and M. V. Ricart, “Morphological study of skin cancer lesions through a 3D scanner based on fringe projection and machine learning.”, *Biomedical Optics Express*, 10(7), pp. 3404-3409, doi:10.1364/boe.10.003404, 2019.
4. Takeda, M., and K. Mutoh, “Fourier transform profilometry for the automatic measurement of 3-D object shapes.”, *Applied Optics*, 22(24), pp. 3977-3982, doi:10.1364/AO.22.003977, 1983.
5. Zhao, H., W. Chen, and Y. Tan, “Phase-unwrapping algorithm for the measurement of three-dimensional object shapes.”, *Applied Optics*, 33(20), pp. 4497-4500, doi:10.1364/ao.33.004497, 1994.
6. Woolford, S., and I. S. Burnett, “Toward a one shot multi-projector profilometry system for full field of view object measurement.”, *IEEE International Conference on Acoustics, Speech and Signal Processing (ICASSP)*, pp. 569-573, doi:10.1109/icassp.2014.6853660, 2014.
7. Abramovici, A., Althouse, W. E., Drever, R. W., Gürsel, Y., Kawamura, S., Raab, F. J., ... & Vogt, R. E. (1992). LIGO: The laser interferometer gravitational-wave observatory. *science*, 256(5055), 325-333.
8. Langenbeck, P. H., “Lloyd Interferometer Applied to Flatness Testing.”, *Applied Optics*, 6(10), pp. 1707-1714, doi:10.1364/ao.6.001707, 1967.
9. Kart, T., G. Köseoğlu, H. Yüksel and M. N. İnci, “Fourier transform optical

- profilometry using fiber optic Lloyd's mirrors", *Applied optics*, Vol. 53, No. 35, pp. 8175–8181, 2014.
10. Wathuthanthr, *Theory of Lloyd's Mirror Interferometer*, 2012, https://www.academia.edu/11430326/Theory_of_Lloyd_s_Mirror_Interferometer, accessed in June 2019.
 11. Grattan, K. T., & Meggitt, B. T. (Eds.). (1995). *Optical fiber sensor technology* (Vol.1). London: Chapman & Hall.
 12. Yuan, L., Y. Liu, and W. Sun, "Fiber optic moiré interferometric profilometry." *Advanced Materials and Devices for Sensing and Imaging II*, 5633, pp. 55-65, doi:10.1117/12.570131, 2005.
 13. Easton, *Waves and Imaging*, 2005, https://www.cis.rit.edu/class/simg712-01/notes/11-Waves_in_imaging.pdf, accessed in June 2019.
 14. Hernández, I. R., Gustavo Rodríguez, Jorge Luis Flores, and Rumen Ivanov, "The 2D Continuous Wavelet Transform: Applications in Fringe Pattern Processing for Optical Measurement Techniques, Wavelet Theory and Its Applications." *IntechOpen*, doi: 10.5772/intechopen.74813, 2018
 15. Sayelje, V., S. K. Kim, and J. Kim, "Moiré effect in displays: A tutorial.", *Optical Engineering*, 57(3), doi:10.1117/1.oe.57.9.099801, 2018
 16. Wang, Z., J. Ma, and M. Vo, "Recent progress in two-dimensional continuous wavelet transform technique for fringe pattern analysis." *Optics and Lasers in Engineering*, 50(8), pp. 1052-1058, doi:10.1016/j.optlaseng.2012.01.029, 2012.
 17. Reddy, V. K., K. K. Siramoju, and P. Sircar, "Object Detection by 2-D Continuous Wavelet Transform.", *2014 International Conference on Computational Science and Computational Intelligence*, 1, pp. 162-167, doi:10.1109/csci.2014.34, 2014.
 18. Antoine, J. P., P. Carrette, R. Murenzi, and B. Piette, "Image analysis with two-dimensional continuous wavelet transform.", *Signal processing*, 31(3), pp. 241-272, doi:10.1016/0165-1684(93)90085-O, 1993.
 19. Arfken GB, Weber HJ. "Mathematical Methods for Physicists" *Academic Press*: Boston, MA, USA, 2005

20. Yılmaz, O. K., "Determination of height profile from a two-dimensional fringe signal using a two-dimensional continuous wavelet transform", *Turkish Journal of Physics*, Vol. 41, No. 1, pp. 81–89, 2017
21. Li, S., X. Wang, X. Su, and F. Tang, "Two-dimensional wavelet transform for reliability-guided phase unwrapping in optical fringe pattern analysis." *Applied Optics*, 51(12), pp. 2026-2034, doi:10.1364/ao.51.002026, 2012.
22. Gates, J. W., "Reverse-Shearing Interferometry.", *Nature*, 176(4477), pp. 359-360, doi:10.1038/176359a0, 1955.
23. Ghosh, N., and K. Bhattacharya, "Cube beam-splitter interferometer for phase shifting interferometry.", *Journal of Optics*, 38(4), pp. 191-198, doi:10.1007/s12596-009-0017-6, 2009.
24. Baumeister, P. W., "Optical Tunneling and Its Applications to Optical Filters.", *Applied Optics*, 6(5), pp. 897-905, doi:10.1364/ao.6.000897, 1967.
25. Kasap, S., and R. K. Sinha, (2013) *Optoelectronics and photonics: Principles and practices*, Prentice Hall, Upper Saddle River, New Jersey, USA, 2013.
26. Drude, P., *The Theory of Optics*, 1902.
27. Kōsters, W., "Interferenzdoppelprisma für Messwecke", *German patent*, p. 59521, 1934.
28. Gao, P., B. Yao, J. Min, R. Guo, J. Zheng, T. Ye, I. Harder, V. Nercissian, and K. Mantel, K. "Parallel two-step phase-shifting point-diffraction interferometry for microscopy based on a pair of cube beamsplitters.", *Optics Express*, 19(3), pp. 1930-1935, doi:10.1364/oe.19.001930, 2011.
29. Ribak, E., and S. G. Lipson, "Complex spatial coherence function: Its measurement by means of a phase-modulated shearing interferometer.", *Applied Optics*, 20(6), p. 1102, doi:10.1364/ao.20.001102, 1981.
30. Ferrari, J. A., and E. M. Frins, "Multi-frequency fringe projection profilometry based on wavelet transform.", *Optics Communications*, 279(2), pp. 235-239, doi:10.1016/j.optcom.2007.07.038, 2007.
31. Pokorski, K., & Patorski, K. "Separation of complex fringe patterns using two-dimensional continuous wavelet transform", *Applied optics*, 51(35), 8433-8439, 2012.

32. Jacques, L., A. Coron, P. Vandergheynst and A. Rivoldini, *The YAWTb toolbox : Yet Another Wavelet Toolbox*, 2017, <http://sites.uclouvain.be/ispgroup/yawtb>, accessed in June 2019.
33. Luong, B., *Costantini phase unwrapping - File Exchange - MATLAB Central*, 2009, <https://www.mathworks.com/matlabcentral/fileexchange/25154-costantini-phase-unwrapping?requestedDomain=www.mathworks.com>, accessed in July 2019.
34. Kasim, M. F., *2D Weighted Phase Unwrapping - File Exchange - MATLAB Central*, 2016, <https://www.mathworks.com/matlabcentral/fileexchange/60345-2d-weighted-phase-unwrapping?focused=7094234&tab=function>, accessed in July 2019.